Improvement of Antenna System of Interferometric Microwave Imager on WCOM

Aili Zhang[1, 2], Hao Liu[1, *], Xue Chen[1], Lijie Niu[1], Cheng Zhang[1], and Ji Wu[1, 2]

Abstract—The interferometric synthetic aperture microwave imager (IMI) on WCOM is a one-dimensional L/S/C tri-frequency microwave radiometer aiming to improve the measurement capability on soil moisture and ocean salinity. An IMI antenna system mainly consists of a parabolic cylinder reflector and a tri-frequency linear patch feed array. At present, an L-band ground prototype with a solid reflector and an 8-element feeds array is completed, with the imaging feasibility being verified by experimental results. In order to improve radiometer imaging performance, this paper presents an improved antenna system, which is dedicated to the next generation of interferometric microwave imager prototype. Improvements made for the antenna system mainly include using deployable mesh reflector and increasing antenna feeds. Simulation results of image reconstruction in viewing a series of near real case ocean brightness temperature maps are used to quantitatively compare and analyze imaging performances of the two L-band IMI prototype antenna systems.

1. INTRODUCTION

The Water Cycle Observation Mission (WCOM) is an earth science mission dedicated to synergetic observations of global water cycle parameters, with emphasis on soil moisture, ocean surface salinity, snow water equivalent and frozen/thaw [1]. In order to satisfy these measurement requirements, WCOM is equipped with payloads in combination of active and passive microwave sounding capabilities of frequency from L-band to W-band. One of the three payloads onboard WCOM is an interferometric synthetic aperture microwave imager (IMI), which is a tri-frequency passive remote sensing imager that mainly aims at producing the global sea surface salinity and soil moisture maps [2]. L-band radiometry has been identified as a most effective tool to measure these two parameters from space. At present, three space missions with L-band instruments onboard have already been successfully implemented, including ESA's SMOS mission launched in 2009 with a two-dimensional Y-shape interferometric microwave radiometer named MIRAS [3] and an NASA's Aquarius mission launched in 2011 with a three-beam push-broom radiometer/scatterometer [4] and SMAP mission launched in 2015 with a conical scanning radiometer and SAR [5].

In addition, a ground-based L-band one-dimensional interferometric radiometer demonstrator was developed in NSSC, China during 2012–2015, as shown in Figure 1. Its experimental results have verified the feasibility of the image reconstruction algorithm and evaluated the performance parameters, such as spatial resolution, stability and accuracy [6]. However, the experiment results have also shown that challenges still exist in achieving better imaging accuracy, sensitivities and spatial resolution. In practical applications, these three parameters are very important for the retrieval of sea surface salinity (SSS) and soil moisture. In this paper, in order to obtain better imaging accuracy, sensitivity and spatial resolution, an improved antenna system has been proposed for the next-generation L-band one-dimensional prototype of IMI.

(a)   (b)
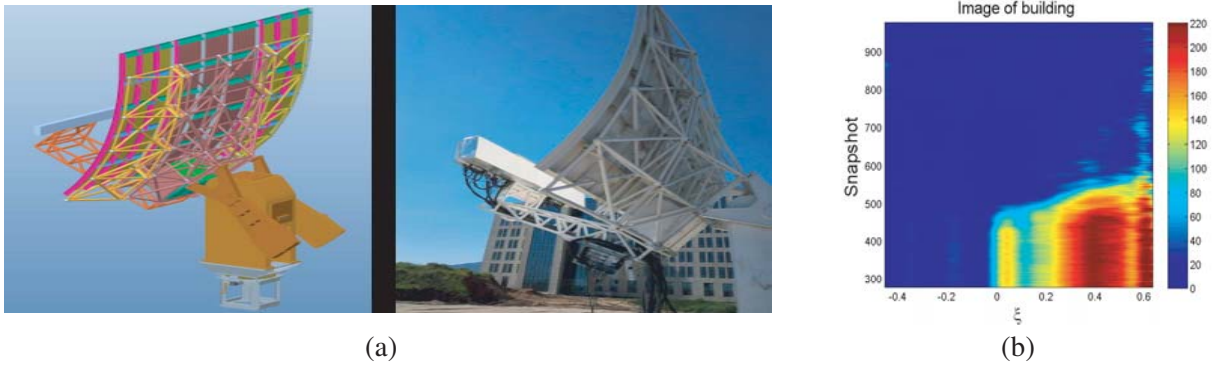
Figure 1. (a) Structural view of L-band 1-D synthetic aperture radiometer prototype. (b) Retrieved image of building.

2. ANTENNA SYSTEMS

The antenna system used in ground prototype and the improved antenna system of IMI are described and compared in detail in this section. For convenience, the two antenna systems are numbered, namely No. 1 and No. 2. The operating frequency of interferometric microwave imager (IMI) is 1.4135 GHz. Its antenna system mainly consists of a parabolic cylinder reflector and a tri-frequency linear patch feed array.

2.1. Antenna System of Radiometer Prototype

In the antenna system of existing ground-based IMI demonstrator, 8 antenna feed elements share a $4.5\,\text{m} * 3\,\text{m}$ solid parabolic cylinder reflector, whose artistic view is shown in Figure 1(a). The specific location of antenna feed patches is: [0 2 4 6 7 8 17 20] in an 8-element linear feed array arrangement, shown as the arrangement of yellow squares in Figure 2. Since this antenna array adopts uniform array arrangement, antenna feed positions are integers. The shortest distance between feeds is set as 0.13 m, which also limits the feed size itself. In this antenna array system, the size of the larger feed is twice the size of the smaller one, as shown in Figure 2. The application of large antenna feeds is aimed at improving the sensitivity of radiometer system. At present, the No. 1 antenna system in the radiometer ground prototype has been completed and put into use. 8 sets of antenna pattern have been measured from actual 8 antenna feeds in the radiometer instrument, as shown in Figure 3. It should be noticed that there are some ripples within the main lobe of antenna patterns. These ripple errors are mainly caused by mutual coupling effects, which should be carefully measured and to be used for image reconstruction process and the analysis of antenna pattern error.

Figure 2. The antenna feed array arrangement of ground-based demonstrator.

2.2. Improved Antenna System

In the L-band one-dimensional interferometric microwave radiometer system, imaging accuracy largely depends on the number of antenna elements. When the synthetic aperture radiometer system adopts the principle of minimum redundant baseline arrangement, the more the antenna elements are, the more easily the imaging accuracy can be improved. On the other hand, the spatial resolution of radiometer system is highly dependent on the size of antenna aperture. The larger the antenna aperture is, the higher the spatial resolution is. Therefore, in order to improve imaging accuracy and spatial resolution
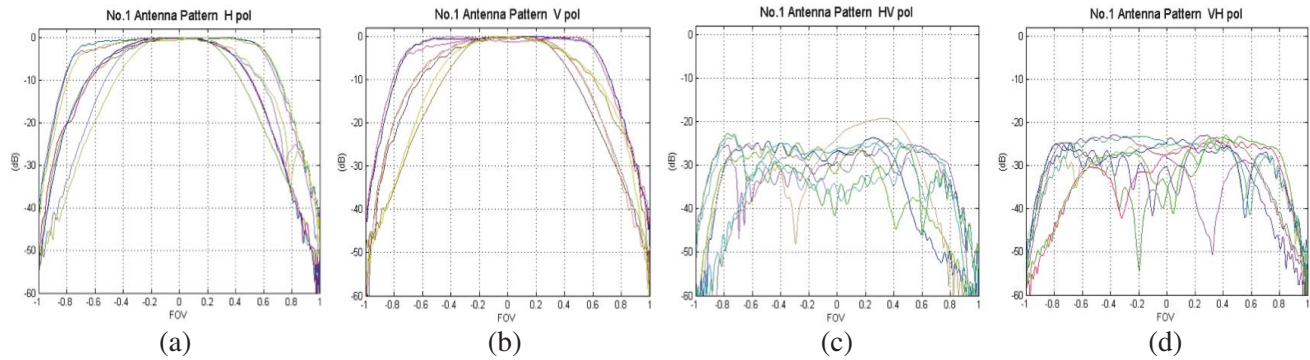
Figure 3. Antenna patterns of 8-element radiometer prototype.

of IMI system, a mesh reflector is used to replace original solid reflector to increase the size of antenna reflector. The structure of improved mesh reflector antenna which will be used in the next generation of IMI prototype is shown in Figure 4. The reflector has good scalability since it consists of a number of framed tetrahedral structure units. The principles of how the tetrahedron structure folds and unfolds is also shown in Figure 4(b). The surface contour of the antenna mesh reflector is a hexagon with a size of $9\,\text{m} * 6\,\text{m}$ in this improved antenna system, which is relatively large. it is still technically feasible to manufacture at L-band and deploy it in space. As the size of the parabolic reflector increases, the length of the antenna feed array also increases. Such changes make it possible to use more antenna feeds in this radiometer system to achieve better brightness temperature image reconstruction. Under the principle that radiometer sampling baselines are continuous and uniform, the improved IMI radiometer antenna feed array arrangement is obtained according to the simulated annealing and genetic algorithm. The improved linear antenna feed array is marked as No. 2, as shown by the red squares arrays in Figure 5. In this case, the new 4 m antenna feed array is arranged as: [0 2 3 6 8 10 12 14 19 20 21 23 26 28 30]. These corresponding 15 antenna patterns are optimized and simulated, as shown in Figure 6.
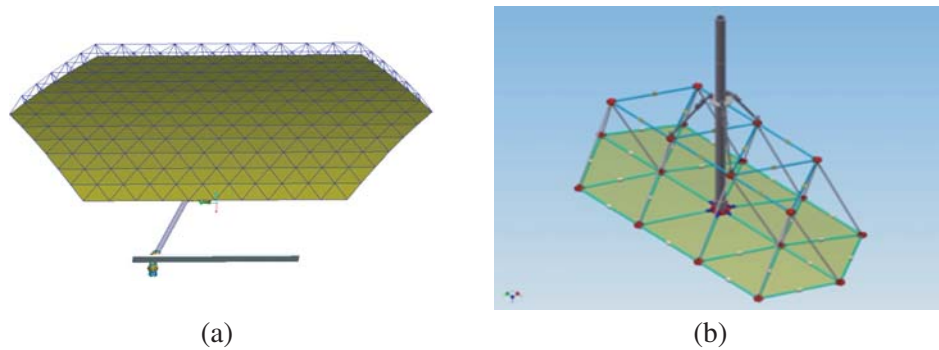

Figure 4. (a) Structural view of improved antenna system in IMI prototype. (b) The tetrahedron structure units in the mesh reflector.

Figure 5. The antenna feed array arrangement of the improved antenna system.

2.3. Comparison of Patterns Data between Two Antenna Systems

Compared to the original ground-based radiometer prototype antenna system, the newly proposed antenna system mainly includes the following two parts of the improvement.
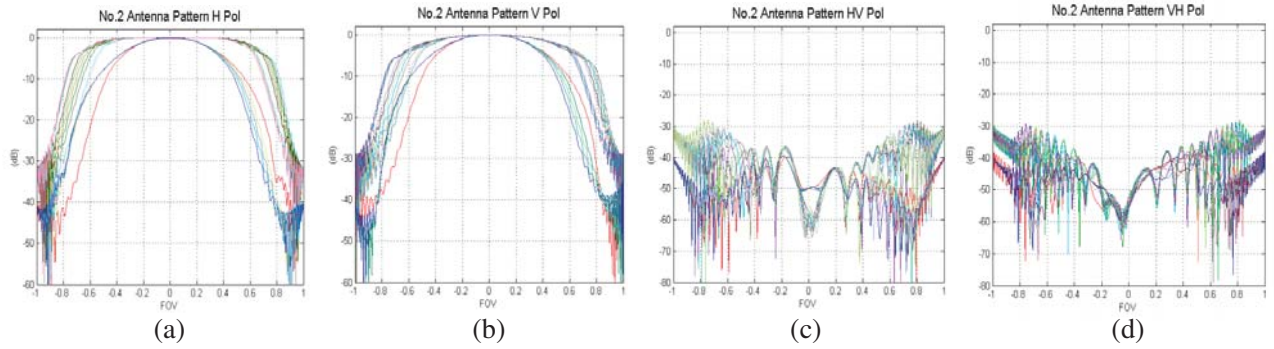
Figure 6. Antenna patterns of 15-element radiometer antenna system.

On the one hand, in the improved antenna system, the use of a mesh reflector increases the size of antenna feed array. With the principle of minimum-redundancy baselines, larger-sized arrays can contain more antenna feed elements. Therefore, the number of feeds in the improved antenna system is almost twice that of the original. The increase of feed elements in the antenna hardware device will greatly improve radiometer imaging quality, including better imaging accuracy, better imaging sensitivity in the Alias-Free Field of View (AF-FOV) and better spatial resolution, which are specifically simulated and described in the following analysis of imaging performance. In this paper, a large number of simulation results are used to study and compare, and these accurate and reliable simulation experiments completely rely on the existing one-dimensional interferometric synthetic aperture radiometer simulator system [7].

On the other hand, comparing patterns data of the two antenna systems in Figure 3 and Figure 6, it can be found that the influence of cross-polarization is smaller, and the consistency between antenna patterns is better. The consistency of antenna patterns is another key factor to reduce brightness temperature image reconstruction error of interferometric synthetic aperture microwave radiometer [8].

3. THE IMPROVEMENT OF RADIOMETER IMAGING PERFORMANCE

In order to quantitatively evaluate the quality of the brightness temperature image reconstruction, the SMOS calibration team agreed the definition of a common metric. It was decided to use the difference between the reconstructed brightness temperature (measured) of the ocean scene and that predicted by the most sophisticated available model [9]. Therefore, in the simulation experiments of this paper, the image spatial bias error is defined as the difference between the reconstructed brightness temperature image and the modeled scene brightness temperature image, which is used to evaluate the imaging accuracy of the radiometer system, shown in Figure 7.

3.1. Quantitative Analysis of Imaging Accuracy

The imaging spatial errors are respectively simulated under the conditions of the improved antenna system and the antenna system from ground radiometer prototype. The imaging simulation results in dual polarizations are shown in Figure 8. Its specific statistical parameters of the imaging spatial errors are listed in Table 1.

The simulation results in Figure 8 show that Gibbs error can be effectively suppressed by increasing the number of feeds of antenna array in the image reconstruction of L-band one-dimensional synthetic aperture radiometer. The reason is that increasing the number of measurement baselines can reduce sampling truncation error in spatial domain. Therefore, the imaging Gibbs error of the antenna system with many elements will be smaller.

However, from the simulation results in Figure 8, we can also find that reconstructed image spatial error is dependent on polarization. There is a bias about $0.5\,\mathrm{K}$ in the H-polarized image spatial error in the No. 2 antenna system. In the actual data processing, we can use differential algorithm to calibrate such an image error bias since it is stable when observation target is always ocean scene. Therefore,
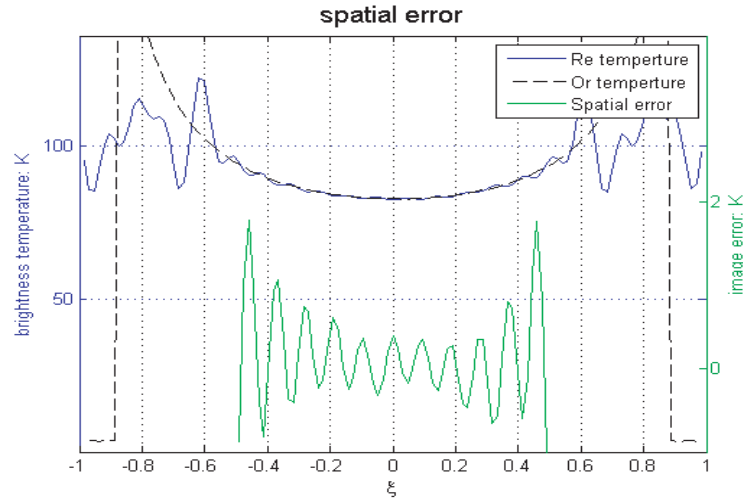
Figure 7. The modeled target brightness temperature image (black curve). Reconstructed brightness temperature image through radiometer observation (blue). The image spatial bias error in the alias free field of view (green).
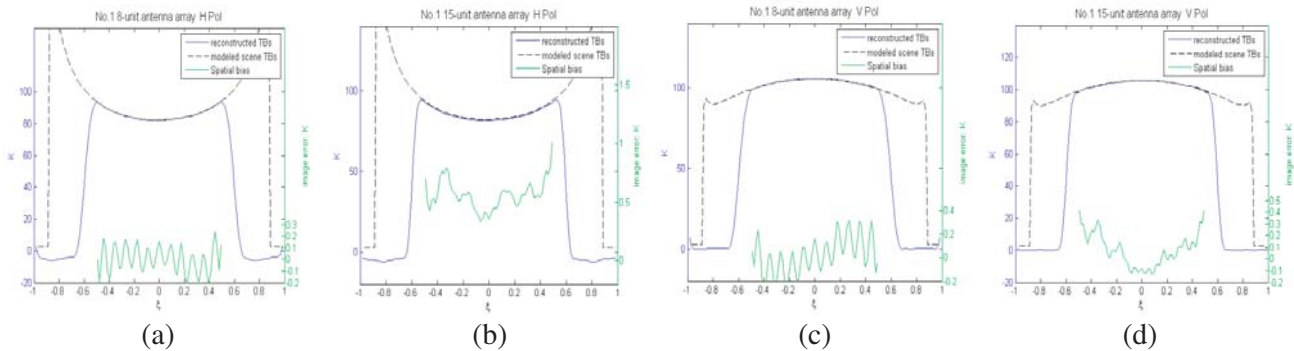

Figure 8. (a) and (b) Simulated image spatial error of 8-element ground experimental prototype in dual polarizations. (c) and (d) Simulated image spatial error of improved antenna system in H and V.

Table 1. Statistical parameters of the image spatial bias.

Antenna array	No. 1	No. 1	No. 2	No. 2
Polarization	H	V	H	V
STD (K)	0.11	0.17	0.11	0.12
MEAN (K)	0.01	0.02	0.55	0.05

the STD parameter of image reconstruction spatial error is used to evaluate imaging accuracy here. Comparing the simulated imaging results of the antenna arrays No. 1 and No. 2 in Table 1, it can be concluded that improvement of antenna system can make radiometer image reconstruction more accurate.

3.2. Quantitative Analysis of Imaging Sensitivity

At present, an L-band 1-D synthetic aperture radiometer ground prototype has been completed. It has made a series of experiments, such as the observation of sun, cold sky, and closer building [6]. Figure 9 shows an experimental image with the selected 300 observed snapshots after the Flat Target
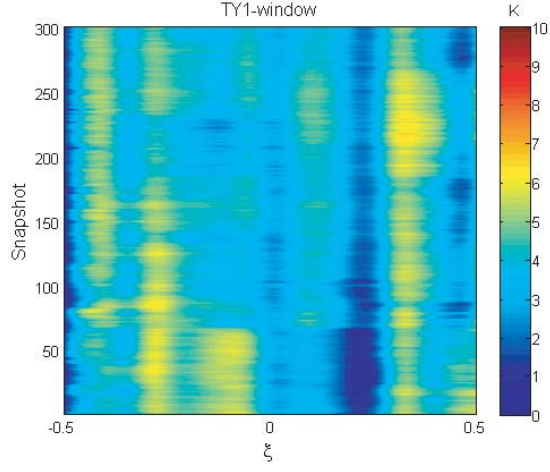
Figure 9. Experimental imaging results of radiometer prototype observation of cold sky.
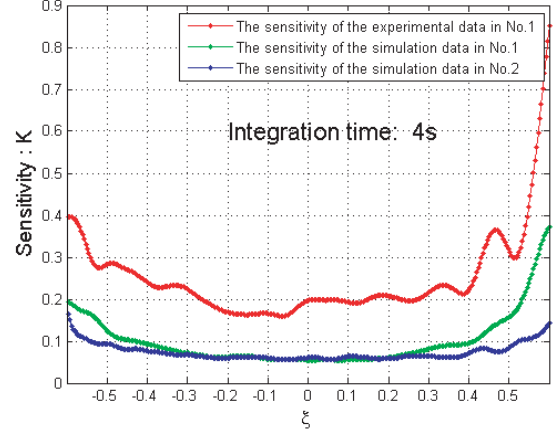

Figure 10. Sensitivity analysis of different fees arrays radiometers.

Transformation (FTT) [10] calibration when the radiometer prototype observes cold sky. In the next data analysis, we use the cold sky observation data to study radiometer imaging sensitivity.

The radiation sensitivity equations of visibilities in the interferometric synthetic aperture microwave radiometer are [11]:

$$\Delta V_r \left(u, v \right) = \frac{1}{\sqrt{2B\tau}} \cdot \sqrt{\left(T_A + T_{R1} \right) \left(T_A + T_{R2} \right) + V_r^2 \left(u, v \right) - V_i^2 (u, v)} \tag{1}$$

$$\Delta V_i \left(u, v \right) = \frac{1}{\sqrt{2B\tau}} \cdot \sqrt{\left(T_A + T_{R1} \right) \left(T_A + T_2 \right) + V_i^2 \left(u, v \right) - V_r^2 (u, v)} \tag{2}$$

ΔV_r is the real part of radiation sensitivity of visibilities, and ΔV_i is the imaginary part of radiation sensitivity of visibilities.

According to radiation sensitivity equations of visibility function, the sensitivity of cold sky data is simulated. The simulation experiment assumes that receiver temperature $T_r = 300\,\text{K}$, antenna brightness temperature $T_A = 10\,\text{K}$, bandwidth $B = 25\,\text{M}$, and integration time $\tau = 4\,\text{s}$. The settings of these parameters are consistent with actual experimental data of prototype. When integral time is set as 4 seconds for cold sky observation, the results of sensitivity are shown in Figure 10. The red curve is sensitivity of experimental cold-sky observation data. The green and blue curves in Figure 10 are respectively the simulated sensitivity results of the No. 1, No. 2 feed arrays. After analyzing and comparing the experimental and simulated sensitivity curves (red curve and green curve) for the No. 1 8-unit antenna feed array, it is found that these two curves have approximately the same outlines yet differ by about 0.2 K in magnitude. This difference is caused by instrument internal calibration link because radiometer's signal channels are not perfectly ideal. Comparing the simulated sensitivity curves (green curve and blue curve) for these two antenna systems, the sensitivity parameter of No. 2 antenna feed array is more optimized in the entire alias-free field of view.

3.3. Quantitative Analysis of Spatial Resolution

The spatial resolution of radiometer depends on the size of actual aperture of cylinder reflector in follow-track direction. In the cross-track direction, spatial resolution of radiometer is determined by the synthetic aperture length of the sparse feed array. Therefore, the spatial resolution of the new feed arrays is twice that of the No. 1 feed array, in the real aperture direction. Table 2 shows the longest sampling baselines of two groups of antenna feed arrays in spatial frequency domain and the spatial resolution without windowing function, when the orbit height is 650 km. The du represents the shortest distance between antenna feeds, and du in each antenna feed arrays is equal to 0.13 m.

Table 2. Statistical parameters of the simulation.

	No. 1	No. 2
Longest continuous baseline	18 du	28 du
Spatial resolution	37.46 km	24.22 km

4. CONCLUSION

In this paper, two sets of linear antenna systems are presented for the L-band one-dimensional synthetic aperture radiometer. One is the antenna of the IMI ground prototype, and the other is the improved antenna system after applying the mesh technology. By quantitatively comparing and analyzing the imaging quality of the two antenna systems, it can be seen that the improved radiometric antenna system is more conducive to improving imaging accuracy, sensitivity and spatial resolution. Specifically, since the aperture of the improved mesh antenna is increased, the radiometric imaging has a better spatial resolution. Moreover, in the improved antenna system, as the antenna reflector becomes larger, the number of antenna feeds increases, which helps to optimize the accuracy and sensitivity of radiometer imaging. So the newly improved radiometer antenna system is more suitable for the next generation L-band prototype of IMI.

ACKNOWLEDGMENT

REFERENCES

1. Shi, J., et al., "Snow water equivalent monitoring from dual-frequency scatterometer on WCOM," *2017 IEEE International Geoscience and Remote Sensing Symposium (IGARSS)*, 1359–1362, Fort Worth, TX, 2017.
2. Liu, H., et al., "IMI (Interferometric Microwave Imager): A L/S/C tri-frequency radiometer for Water Cycle Observation Mission(WCOM)," *2016 IEEE International Geoscience and Remote Sensing Symposium (IGARSS)*, 3445–3447, Beijing, 2016.
3. Corbella, I., et al., "MIRAS calibration and performance: Results from the SMOS in-orbit commissioning phase," *IEEE Transactions on Geoscience and Remote Sensing*, Vol. 49, No. 9, 3147–3155, Sept. 2011.
4. Le Vine, D. M., G. S. E. Lagerloef, F. R. Colomb, S. H. Yueh, and F. A. Pellerano, "Aquarius: An instrument to monitor sea surface salinity from space," *IEEE Transactions on Geoscience and Remote Sensing*, Vol. 45, No. 7, 2040–2050, Jul. 2007.
5. Piepmeier, J. R., et al., "SMAP L-BAND MICROWAVE RADIOMETEr: Instrument design and first year on orbit," *IEEE Transactions on Geoscience and Remote Sensing*, Vol. 55, No. 4, 1954–1966, Apr. 2017.
6. Niu, L., H. Liu, L. Wu, and J. Wu, "Experimental study of an L-band synthetic aperture radiometer for ocean salinity measurement," *2016 IEEE International Geoscience and Remote Sensing Symposium (IGARSS)*, 418–421, Beijing, 2016.
7. Zhang, A., H. Liu, J. Wu, and L. Wu, "Antenna pattern error calibration for L-band synthetic aperture radiometer," *2017 IEEE International Geoscience and Remote Sensing Symposium (IGARSS)*, 500–503, Fort Worth, TX, 2017.
8. Martín-Neira, M., et al., "SMOS instrument performance and calibration after six years in orbit," *Remote Sensing of Environment*, Vol. 180, No. 8, 19–39, 2016.

9.   Corbella, I., F. Torres, L. Wu, N. Duffo, I. Durán, and M. Martín-Neira, "Spatial biases analysis and mitigation methods in SMOS images," *2013 IEEE International Geoscience and Remote Sensing Symposium (IGARSS)*, 3415–3418, Melbourne, VIC, 2013.

10. Martin-Neira, M., M. Suess, J. Kainulainen, and F. Martin-Porqueras, "The flat target transformation," *IEEE Transactions on Geoscience and Remote Sensing*, Vol. 46, No. 3, 613–620, Mar. 2008.

11. Ruf, C. S., C. T. Swift, A. B. Tanner, and D. M. Le Vine, "Interferometric synthetic aperture microwave radiometry for the remote sensing of the Earth," *IEEE Transactions on Geoscience and Remote Sensing*, Vol. 26, No. 5, 597–611, Sept. 1988.